Evolution of the edge states and corner states in a multilayer honeycomb valley-Hall topological metamaterial

Tao, Liyun; Liu, Yahong; Du, Lianlian; Li, Meize; Yuan, Xin; Xiao, Xiang; Navarro-Cia, Miguel; Zhao, Xiaopeng

DOI:
10.1103/PhysRevB.107.035431

Evolution of the edge states and corner states in a multilayer honeycomb valley-Hall topological metamaterial

Liyun Tao,[1] Yahong Liu,[1,*] Lianlian Du,[1] Meize Li,[1] Xin Yuan,[1] Xiang Xiao,[1] Miguel Navarro-Cía,[2,3] and Xiaopeng Zhao[1]

[1]*School of Physical Science and Technology, Northwestern Polytechnical University, Xi'an 710129, People's Republic of China*

[2]*School of Physics and Astronomy, University of Birmingham, Birmingham B15 2TT, England, United Kingdom*

[3]*Department of Electronic, Electrical, and Systems Engineering, University of Birmingham, Birmingham B15 2TT, England, United Kingdom*

(Received 19 October 2022; accepted 11 January 2023; published 24 January 2023)

The valley-Hall effect provides topological protection to a broad class of defects in valley-Hall photonic topological metamaterials. Unveiling precisely how such protection is achieved and its implications in practical implementations is paramount to move from fundamental science to applications. To this end, we investigate a honeycomb valley-Hall topological metamaterial and monitor the evolution of the topological valley-Hall edge states and higher-order corner states under different perturbation δR. The evolutions of the edge states of the armchair and zigzag interfaces are demonstrated, respectively. By adjusting the geometric parameters and introducing disturbances to break the inversion symmetry, we achieve the edge states with different modes including the conventional crossed edge state and the specific gapped edge state. It is found that the edge states of topological valley kinking will gradually separate with the increase of δR, and finally a complete gap between the edge states appears. The gap has rarely been reported previously in topological materials fabricated by printed circuit board technology. In addition, the higher-order topological corner states can also be observed in the proposed topological metamaterial. The higher-order topological phase is theoretically characterized by nontrivial bulk polarization and the Wannier centers. Our results show that the corner state localization becomes stronger with the increase of δR. It is expected that our results will provide a platform for the realization of optical topological insulators.

DOI: 10.1103/PhysRevB.107.035431

I. INTRODUCTION

Topological insulators (TIs) opened up an avenue for the study of matter phases and have become an important branch in condensed matter physics [1–4]. The boundary mode of TIs can show the characteristics of lossless and robust transmission, which has been experimentally verified in physical systems such as photonics [5–8], microwaves [9–11], electric circuits [12,13], mechanics [14], and acoustics [14–17]. With the discovery of lower-dimensional topological corner states and hinge states, higher-order TIs have been proposed, which breaks the traditional bulk-boundary correspondence. Higher-order TIs correlate with the overall properties of materials and topological bulk polarization, bringing a new method to realize topological phases in higher dimensions [10,18–25].

Valley-Hall TIs have been intensively explored as a convenient research platform for implementing topological materials in recent years [25–32]. "Valley" refers to the quantum states with the energy extremum in the reciprocal space. A pair of degenerate but not equivalent energy extremes in the momentum space, called a valley, is one of the two high symmetry points (K and K') in the first Brillouin zone (FBZ). It is demonstrated that topological valley kink edge states emerge at the interface between opposite valley-Chern number (VCN) regions. It is shown that the topological valley kinks exist at the interfaces including zigzag, armchair, and any combinations of the zigzag and armchair interfaces. The edge states are characterized by the different VCN of the interfaces. In two-dimensional systems, introducing geometric perturbation to break inversion symmetry of the crystal structure can lead to the appearance of opposite Berry curvature (BC) in the K/K' valley of the band structure, where the two valleys are called "pseudospin" degrees of freedom. Thus, the crystal structure with opposite VCN is constructed, and edge states can be observed [33,34].

Recently, topological edge states from honeycomb photonic crystals to triangular-lattice photonic crystals by changing the radius of the air hole have been explored. It is shown that valley edge states can exist even if BC vanishes [35]. A fully gapped regime has been reported in valley-Hall topological edge states by varying the refractive index in evanescently coupled waveguide arrays [36]. This specific gapped edge state is interesting and different from the conventional crossed edge state. However, the physical mechanism to achieving a gapped edge state needs to be demonstrated clearly. Valley-selective topological corner states have also been experimentally realized in two-dimensional sonic crystals [37]. The topological corner states can be selectively switched, which provides a fundamental understanding of the interaction between higher-order topology and the valley degrees of freedom. In our previous work, we have also achieved an edge

*Corresponding author: yhliu@nwpu.edu.cn

state with a gapped region in mechanically reconfigurable valley-Hall topological metamaterials [38]. Although great achievements have been made in topological edge states and corner states, it is still a challenge to achieve the evolvement rule of the different edge states from the conventional crossed edge state to the fully gapped edge state. It will provide a new mechanism for the realization of time-reversal-invariant photonic TIs. In addition, it is unclear whether the energy local intensity of the higher-order corner states can be tuned by geometric perturbations in honeycomb lattice photonic TIs.

In this paper, we propose a honeycomb valley-Hall topological metamaterial with multilayer structure fabricated by printed circuit board technology, which is a perfect platform for constructing valley-Hall TIs. By varying the geometric structural parameters and introducing perturbation δR to break the inversion symmetry and open the Dirac degeneracy point at the K/K' valley, which induce the bulk gap, topological valley-Hall edge states and higher-order corner states can be realized. First, we demonstrate the evolution of the valley edge states at the armchair and the zigzag domain walls with different perturbation factors δR in honeycomb lattice topological metamaterial. The edge states with different modes including the conventional crossed edge state and specific gapped edge states can be obtained. We achieve the separated valley edge states as δR increases, showing a fully gapped regime in the edge states. This unique regime is rarely reported in two-dimensional honeycomb TIs fabricated by using printed circuit board technology. Second, we characterize the nontrivial bulk polarization and the Wannier centers in the proposed structure. The triangular supercells are surrounded by the valley-Hall topological metamaterials with opposite VCN implemented. Higher-order corner states with different modes are obtained. It is shown that the higher-order corner states without valley selectivity are obtained, and it is notable that the energy local intensity of the higher-order corner states can be tuned by the perturbation factors δR. The experimental results are in good agreement with theoretical analysis. It is expected that we will provide a mechanism for the realization of valley-Hall topological TIs.

II. MODEL AND THEORETICAL ANALYSIS

The proposed structure consists of three stacked layers of dielectric plates as illustrated in Fig. 1(a). The substrate is a traditional $t = 0.508$ mm thick high-frequency dielectric material F4B with a relative permittivity of 4.4 and loss tangent of 0.025. Metallic copper patterns with a thickness of 0.035 mm are deposited on one side of the F4B. The copper pattern of the bottom layer is honeycomb composed of two kinds of circular patches with the radii of R_1 and R_2, respectively. The middle layer is a snowflake shape, composed of six regular hexagons with side length l connected by a rod with the width l_1 and length l_2. The top layer structure is exactly the same as the bottom layer. There is no air gap between each layer. The diagram of the proposed unit cell is shown in Fig. 1(b), where the upper right panel displays the FBZ of the honeycomb lattice. As $R_1 = R_2 = 1.75$ mm, the unit cell has mirror symmetry along the direction of the high symmetry points ΓK, and the structure has C_6 symmetry.

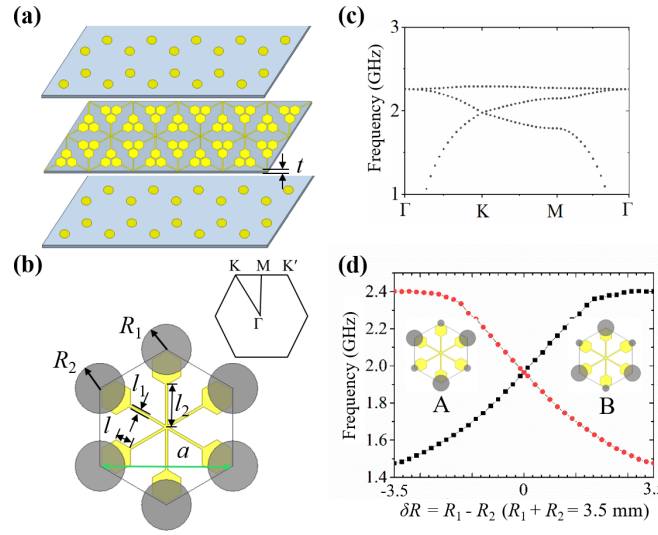

FIG. 1. (a) Schematic illustration of the valley lattice structure consisting of three layers. Metallic patterns are shown (indicated by yellow) on a dielectric F4B substrate (indicated by dark gray) with a thickness of $t = 0.508$ mm. (b) Top view of the unit cell. Geometry parameters are shown as $a = 16$ mm, $l = 2$ mm, $l_1 = 0.3$ mm, and $l_2 = 7$ mm. The radii of the two kinds of metallic circular patch are R_1 and R_2, respectively. The top right corner inset shows the Brillouin zone. (c) Band diagram of the structure with $R_1 = R_2 = 1.75$ mm. (d) Eigenfrequencies of the K/K' point and TE modes as a function of δR ($\delta R = R_1 - R_2$, $R_1 + R_2 = 3.5$ mm). $\delta R < 0$ and $\delta R > 0$ correspond to structure A and structure B, respectively. The inversion of frequency indicates a topological phase transition as δR crosses zero.

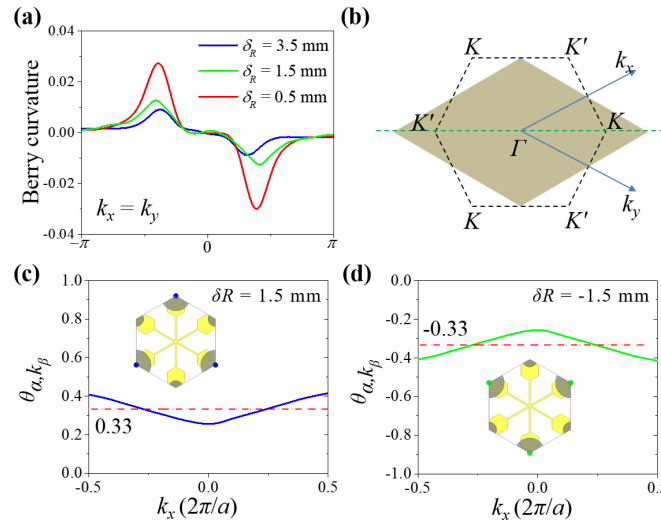

FIG. 2. (a) Calculated Berry curvature of structure B along the line $k_x = k_y$. (b) A rhombic Brillouin zone in the calculation of the bulk polarization, which shares the same area with the original hexagonal Brillouin zone. The green dotted line indicates $k_x = k_y$ in the reciprocal space. (c, d) Calculated Berry phase of (c) $\delta R = 1.5$ mm and (d) $\delta R = -1.5$ mm. Bulk polarization is obtained by the integration of θ_{α,k_β} over k_y. Red dashed lines show the exact values of $1/3$ and $-1/3$. The corresponding Wannier centers are marked by the blue dots and green dots, respectively.

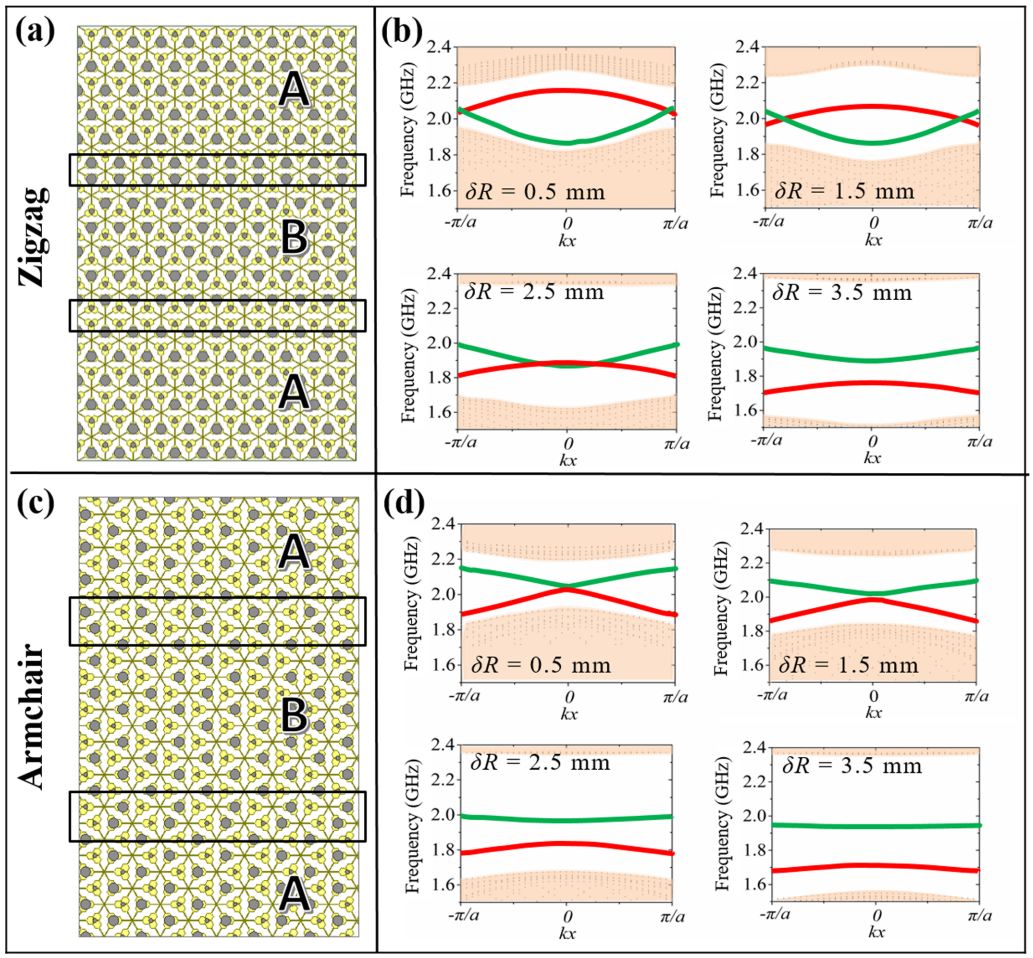

FIG. 3. Schematic diagram of inversion-symmetry-broken honeycomb lattices with (a) zigzag and (c) armchair domain walls. The black solid line regions indicate the domain walls. Two valley topological structures are marked by *A* and *B*. (b, d) Corresponding band structures of the (b) zigzag and (d) armchair edge domain walls with different δR ($\delta R = 0.5$, 1.5, 2.5, and 3.5 mm). Red and green solid lines show the edge states of *AB*-type and *BA*-type domain walls, respectively. The shaded regions represent the projection of the bulk bands.

The dispersion diagram of the FBZ of the proposed crystal structure is obtained by using the commercial software Ansys HFSS as shown in Fig. 1(c). It can be observed that the first band and second band linearly cross at the K/K' valley, forming a Dirac degenerate point. By varying the radius of R_1 and R_2, we introduce a perturbation factor $\delta R = R_1 - R_2$, resulting in changing the degeneracy at the K/K' valley point, and in turn yielding a band gap. The reference radius $R = \frac{R_1+R_2}{2}$ ($R = 1.75$ mm) is a constant for comparison. Figure 1(d) shows the eigenfrequencies dispersion of the K/K' valley in the honeycomb lattice with various δR. $\delta R < 0$ and $\delta R > 0$ correspond to the crystal structure *A* and *B*, respectively. When δR is nonzero, the K/K' valley will become nondegenerate. The nondegenerate circularly polarized states of the K/K' valley will not mix, because the C_3 symmetry of the crystal structure is unchanged under perturbation. The frequency sequence of the polarization states at the K/K' valley is reversed as δR shifts from a negative value to a positive value through the zero point, indicating the topological phase transition. The band gap widens with the increase of δR. A slight variation of R_1 and R_2 can cause the honeycomb lattice's inversion symmetry to be broken and the band gap to be opened.

In order to analyze and demonstrate the difference of the valley-Hall topological phase, we numerically calculate the BC of the first band with different δR. It is known that the VCN of band n is defined by [39]

$$c_n = \frac{1}{2\pi i} \int_{T^2} d^2\, k\, F_\mu(k) \tag{1}$$

where the BC is defined by

$$F_\mu(k) = \partial_k \times i \langle E_k | \partial_k E_k \rangle. \tag{2}$$

The BC can be calculated directly based on the finite element method, whereby we choose the rhomboid Brillouin zone containing the K/K' valley. The BC is obtained by discretizing the integral of the rhomboid Brillouin zone. The calculated BC curves along the $k_x = k_y$ line in the reciprocal space are shown in Fig. 2(a), where the BC curves with different disturbance factors δR ($\delta R = 0.5$, 1.5, and 3.5 mm) are represented by the different colors. It can be seen that the BC value is mainly focused at the K/K' valley, and the absolute values of BC around the K/K' decrease with the increasing of δR. As long as the quantum states are valley

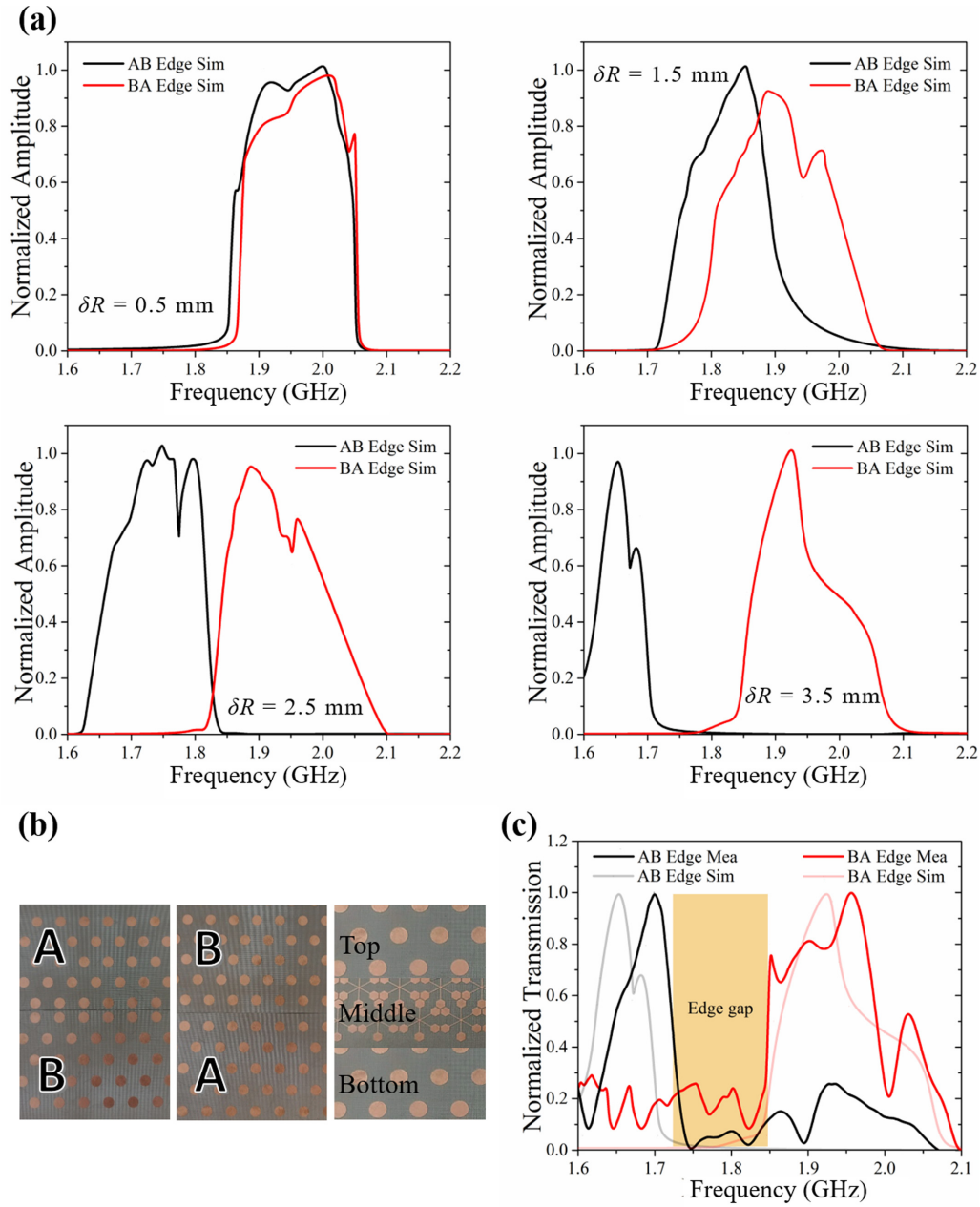

FIG. 4. (a) Simulated transmission of the zigzag domain walls with different δR. (b) Top view of the fabricated samples of the *AB*-type and *BA*-type domain wall with $\delta R = 3.5$ mm. In order to clearly show the proposed sample, the right panel shows three layers of lattice structure (top layer, middle layer, and bottom layer). (c) Measured and simulated transmission for the *AB*-type and *BA*-type zigzag domain walls.

shaped and BCs are opposite at the K and K', the topological phase will be protected by valley topology invariants. These results indicate that the proposed structure is a valley-Hall topological metamaterial as δR is nonzero.

The higher-order topological phase is theoretically characterized by nontrivial bulk polarization and the Wannier centers. In order to better explore the properties of the higher-order corner states, the topological invariants of bulk polarization are calculated. In the two-dimensional system, the expression of the topological phase of the bulk polarization is presented as follows [10]:

$$P_\alpha = -\frac{1}{(2\pi)^2}\int_{BZ} d^2k \mathrm{Tr}[\hat{\wedge}_\alpha],\ \cdots \alpha = x,\ y \tag{3}$$

where $[\hat{\wedge}_\alpha]$ is the Berry connection matrix, which characterizes the relationships between various bands. The matrix elements are expressed as follows:

$$(\hat{\wedge}_\alpha)_{m,n}(k) = i\,\langle u_m(k)|\,\partial_{k_\alpha}\,|u_n(k)\rangle,\ |u_m(k)\rangle \tag{4}$$

where $|u_m(k)\rangle$ is the periodic part of the Bloch function of the m band, and m and n run over the bands below the considered band gap. The bulk polarization is associated with the Wannier centers, and the bulk polarization can be obtained by solving the Wilson loop numerically as follows [37,40]:

$$P_\alpha = -\frac{1}{2\pi}\int_L d\,\theta_{\alpha,k_\beta},\ \cdots \alpha = x,\ y,\quad \beta = x,\ y \tag{5}$$

where L denotes the projection length of the Brillouin zone along the k_β direction. θ_{α,k_β} is the Berry phase along the loop k_α for a fixed k_β. By transforming a hexagon Brillouin zone into a rhombus as shown in Fig. 2(b), when $\delta R < 0$, the bulk polarization can be obtained as $(P_x,\ P_y) = (1/3,\ 1/3)$ for structure A as shown in Fig. 2(c). As $\delta R > 0$, the bulk polarization can be accordingly obtained as $(P_x,\ P_y) = (-1/3,\ -1/3)$ for structure B as presented in Fig. 2(d). Bulk polarization $(P_x,\ P_y)$ represents the Wannier center. Since structure A has the opposite Berry curvature to structure B, which leads to the topological phase transition and inversion of the energy band between the two structures of A and B, the Wyckoff positions of structure A and structure B are opposite. $(P_x,\ P_y)$ reveals that the Wannier centers are located at the Wyckoff position, as presented by the blue and green dots in the insets of Figs. 2(c) and 2(d), respectively. This demonstrates a typical valley-locking property.

III. EVOLUTION OF THE TOPOLOGICAL EDGE STATES

As the inversion symmetry of the lattice is broken, the degeneracy at the Dirac cone is lifted, and propagation modes appear at the interface of two crystal structures with different perturbations, which ensures the existence of topological edge states. We construct *AB*-type or *BA*-type domain walls by using structure A and structure B, and the two domain walls will lead to a pair of topological kink edge states around the K/K' valley. Since the variation of VCN on the domain wall is related to the existence of backpropagation edge states, the pair of kinking edge states is restricted to different valleys, and their propagation directions along the interface are completely opposite, showing "valley-lock" chirality [34–40]. As shown in Figs. 3(a) and 3(c), the *AB*-type and *BA*-type domain walls of the armchair and zigzag are constructed, respectively. The topological kink edge states intersect at the middle frequency of the first gap. Figure 3(b) displays the calculated dispersion of the two types of domain walls of the zigzag interface with different δR ($\delta R = 0.5$, 1.5, 2.5, and 3.5 mm). The edge states of the *AB*-type and *BA*-type domain walls are marked by red and green lines, respectively, and the shaded areas represent the projection of bulk bands. Although the edge states of the *AB*-type and *BA*-type domain walls are both in the first band gap, they gradually separate with the increase of δR until a completely edge state gap region appears. As shown in the bottom right panel of Fig. 3(b), there is no intersection between the two edge states' lines as $\delta R = 3.5$ mm. The results show that the inversion symmetry is broken more prominently with the increase of δR. Figure 3(d) displays the calculated dispersion of the armchair interface, which shows the edge states of the armchair *AB*-type and *BA*-type domain walls always have a gap region (without mixing), and the gap region can gradually widen with the increase of δR. The results demonstrate that the valley topology kink edge states of the two different interfaces gradually separate from each other with the increase of δR.

According to the protection of the topological invariants, protected topological edge states will be realized as long as the K/K' valley satisfies the opposite BC. The difference between the armchair and zigzag edge states may be due to the fact that the *AB*-type and *BA*-type domain walls of the armchair interface mix the K and K' valleys. As a result, a small perturbation factor δR can cause the valley kinked edge states to be broken and separated into a band gap. However, the domain walls of the zigzag interface make the K and K' valleys separate from each other in space. Therefore, there must be a large perturbation for a gap region to appear in the edge states.

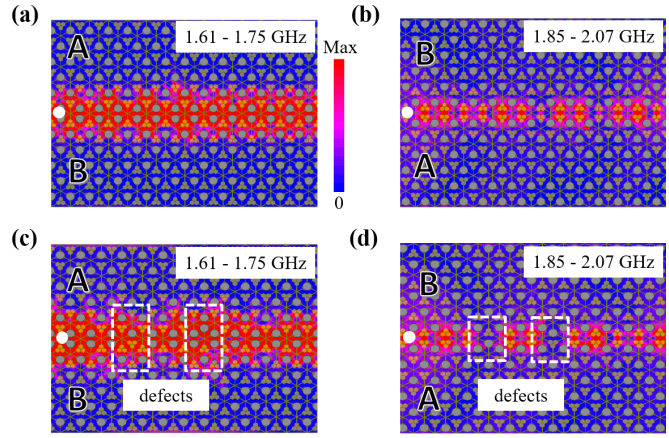

FIG. 5. Simulated electric field distributions of the edge states for the interfaces of (a) *AB*-type zigzag domain wall and (b) *BA*-type zigzag domain wall for $\delta R = 3.5$ mm. The excitation source is depicted by the white dots. Simulated electric field distributions of (c) cavity defects and (d) disorder defects.

In general, the valley-Hall topology edge state is a pair of crossed valley edge states, which has the property of selective transmission [30–35]. However, our proposed multilayer structure can realize the two types of edge states including the crossed valley edge state and the gapped edge state, which is difficult to achieve in the previous optical valley-Hall topological insulators. As compared with the crossed edge state, the gapped edge state provides a greater possibility for the appearance of corner states. The diversity of the edge states' evolution process can provide more degrees of freedom for the manipulation of electromagnetic waves.

As shown in Fig. 4(a), we investigate the transmission of zigzag domain walls with different δR, which can well reveal the evolution process of edge states. The simulated transmission agrees well with the dispersion shown in Fig. 3. In order to experimentally verify the existence of the topological edge states gap, we fabricated the samples of *AB*-type and *BA*-type zigzag interface domain walls with $\delta R = 3.5$ mm, as shown in Fig. 4(b). The measured and simulated normalized transmissions are displayed in Fig. 4(c). It is found that the high transmission is observed at the frequencies of 1.63–1.74 GHz for the *AB*-type domain wall and 1.84–2.05 GHz for the *BA*-type domain wall, respectively. There is an edge gap of 1.74–1.84 GHz between the two high transmission domain walls, indicating a gapped edge state. The slight deviation between the simulations and experiments is due to the tolerance of sample fabrication and the inhomogeneous dielectric constant. In addition, it is unavoidable to have nonperfect contact between layers in the fabricated samples. So, the spacings between multilayer dielectric plates may also cause the slight deviation.

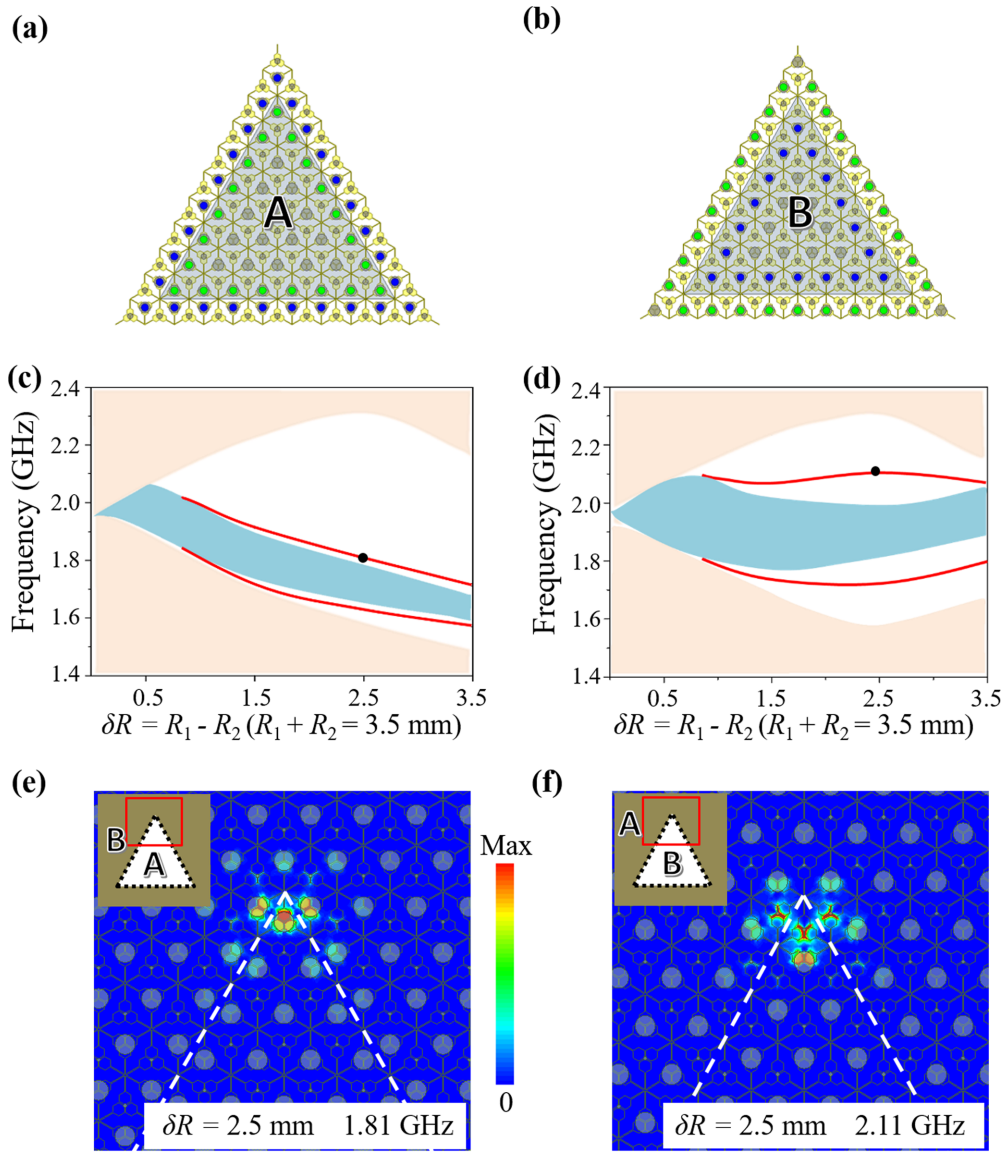

FIG. 6. Schematic views of the zigzag edge triangular corner structures with (a) structure A surrounded by structure B and (b) structure B surrounded by structure A. Wannier centers are illustrated by the green and blue dots. (c) and (d) Eigenfrequencies as functions of the parameter δR of the structure shown in Figs. 6(a) and 6(b). The light pink shaded regions, the light blue shaded regions, and the red solid lines represent the bulk states, the edge states, and the corner states, respectively. (e) and (f) Corner state electric field distributions corresponding to the black dots of Figs. 6(c) and 6(d), respectively. The upper left inset illustration is a schematic of the whole structure.

Figures 5(a) and 5(b) present the simulated electric field diagrams of the edge states of AB type and BA type with $\delta R = 3.5$ mm, respectively. The results show that the electromagnetic wave can carry out perfect transmission at the valley interface domain walls. To characterize the robustness of edge states, as shown in Figs. 5(c) and 5(d), we introduce cavity and disorder defects in the AB and BA domain walls and investigate the transmission. The electric field distributions show that electromagnetic wave can still transmit along the interfaces, indicating the robust transmission.

IV. EVOLUTION OF THE TOPOLOGICAL CORNER STATES

Higher-order corner states break through the unconventional bulk-edge correspondence, and bring a new method to realize topological states in higher dimensions. It can make the bulk states and edge states separate from each other and appear in the gap region between the bulk states and edge states. To investigate the higher-order corner states in our proposed valley topological metamaterial, we construct two types of corner structures with triangular zigzag edge. Structure $A(\delta R > 0)$ arranged in a triangular shape is surrounded by structure $B(\delta R < 0)$ as shown in Fig. 6(a). Structure A surrounds structure B as presented in Fig. 6(b). The configurations of the Wannier centers are represented by the green and blue dots, where the Wannier centers in the bulk cells are hidden for clarification. Setting the perfect electromagnetic boundary conditions in the vertical direction and the periodic boundary conditions in the horizontal direction, the calculated eigenmodes of the two combined structures with different δR

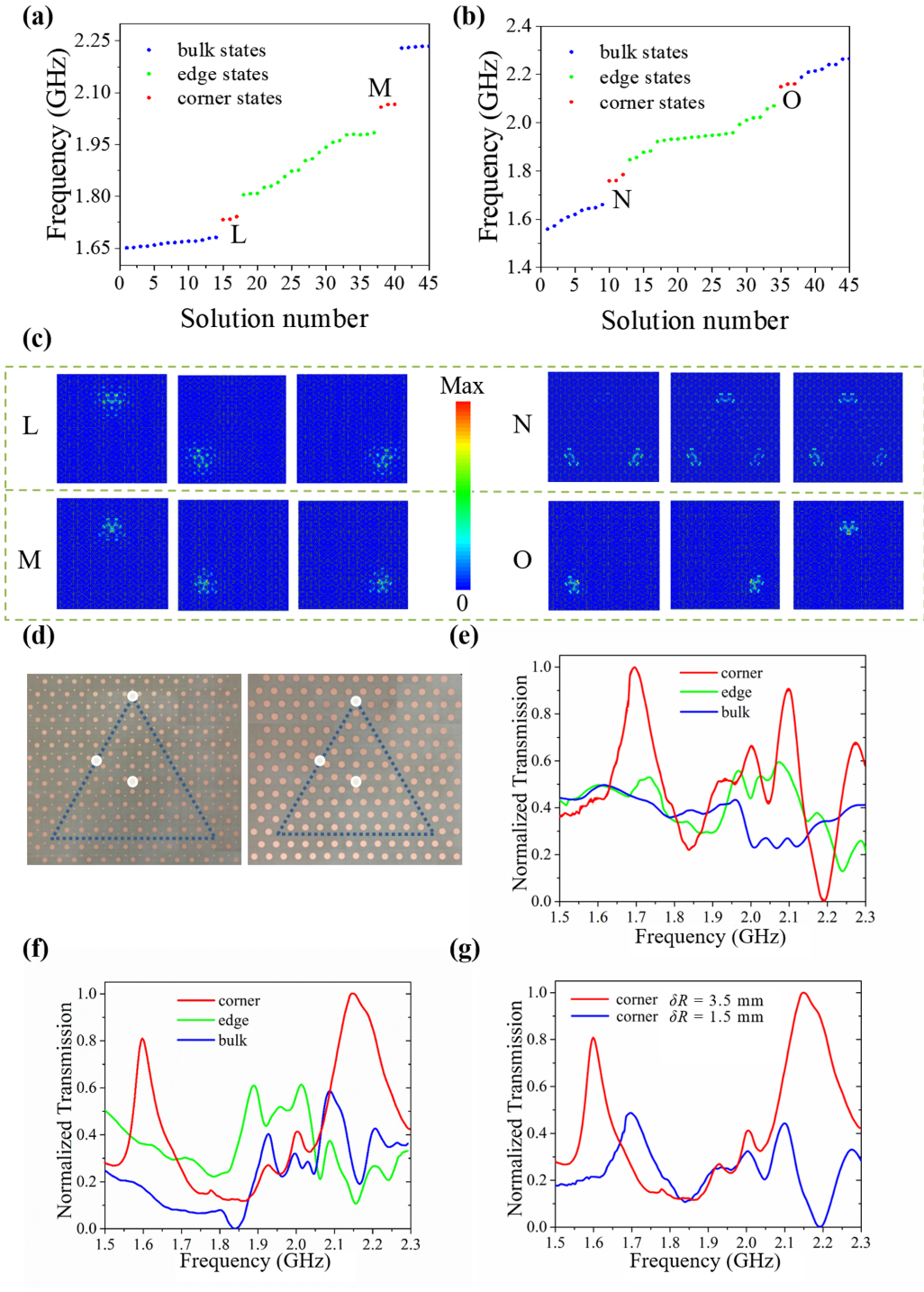

FIG. 7. Eigenmodes of the structure with (a) $\delta R = 1.5$ mm and (b) $\delta R = 3.5$ mm of the triangular corner structures in Fig. 6(d). Corner, edge, and bulk states are represented by red, green, and blue dots, respectively. (c) Electric field distributions of the three degenerate corner states corresponding to L, M, N, and O points. (d) Top view of the fabricated triangular corner structures with $\delta R = 1.5$ mm (left panel) and $\delta R = 3.5$ mm (right panel). White dots indicate the location of the excitation source placed near the corner, edge, and bulk. (e, f) Measured normalized transmissions of (e) $\delta R = 1.5$ mm and (f) $\delta R = 3.5$ mm. (g) Comparative normalized transmission spectra of the corner states with $\delta R = 1.5$ and 3.5 mm.

are shown in Figs. 6(c) and 6(d), respectively. Bulk states, edge states, and corner states are marked as light pink shaded regions, light blue shaded regions, and red solid lines, respectively. As δR is small, the opened band gap is narrow and corner states cannot be separated from bulk states and edge states. However, the topological phase transition occurs between the two structures of A and B as δR is changed from a positive value to a negative value or from a negative value to a positive value. As long as the sign of δR does not change, the Wannier center position remains unchanged. Therefore,

as δR is a small value, the edge states are gapless and the higher-order corner states cannot appear in the bulk band gap. There only exist edge states in the structure with small δR. As the value of δR increases, there exist higher-order corner states in the edge band gap, and the dispersions present the bulk-corner-edge-corner-bulk states. The higher-order corner states appear in the band gap between the edge states and the upper and lower bulk states, including three degenerate corner states at the approximate frequency.

In order to clearly show the corner state characteristics of the two structures, we simulated the electric field distributions of the different triangular structures as shown in Figs. 6(e) and 6(f), respectively. Figure 6(e) is the electric field pattern of $\delta R = 2.5$ mm at 1.81 GHz corresponding to the black dot in Fig. 6(c). Figure 6(f) presents the electric field pattern of $\delta R = 2.5$ mm at 2.11 GHz corresponding to the black dot in Fig. 6(d). It is shown that the electric field distributions of the corner states are well localized at the Wannier centers of the corner of the domain walls. However, the corner states of two types of corner structures can be clearly distinguished, and they are consistent with the theoretical calculation.

Figures 7(a) and 7(b) present the eigenmodes of the structures (A surrounding B) with $\delta R = 1.5$ and 3.5 mm, respectively. Figure 7(c) displays the simulated electric field distributions of the degenerate corner states, clearly showing that the electric field distributions are perfectly confined to the corners of the topological interface. It is shown that the electric field pattern of the corner states becomes more localized with the increase of δR. To analyze the corner states experimentally, we fabricated the samples with $\delta R = 1.5$ mm (left panel) and $\delta R = 3.5$ mm (right panel) as shown in Fig. 7(d). The measured transmission spectra of the two structures are presented in Figs. 7(e) and 7(f), respectively. The measured results are in full agreement with the simulations. By verifying the energy value of the corner states with different δR, Fig. 7(g) displays the comparative transmission spectra of the corner states with $\delta R = 1.5$ and 3.5 mm. It shows that there are two corner states corresponding to the normalized transmissions of 0.48 and 0.42 at the frequencies of 1.69 and 2.09 GHz for the triangular structure of $\delta R = 1.5$ mm. For the triangular structure of $\delta R = 3.5$ mm, two corner states are observed at the frequencies of 1.58 and 2.14 GHz corresponding to the normalized transmissions of 0. 82 and 0.98. The transmission amplitude of $\delta R = 3.5$ mm is twice that of $\delta R = 1.5$ mm. The result indicates that the larger δR the larger the transmission. This measured result agrees with the simulated electric field patterns shown in Fig. 7(c).

V. CONCLUSIONS

We have theoretically and experimentally implemented a two-dimensional valley-Hall topological metamaterial. It is demonstrated that rich one-dimensional edge states and higher-order corner states are obtained by varying δR. We separate the valley kink edge states to realize a complete gap between the edge states. In addition, the higher-order corner states can be achieved, and the energy localization of the corner states becomes more concentrated by adjusting geometrical parameters. The evolution of the topological states enriches the research mechanism of valley-Hall TIs. The proposed mechanism can also be extended to optical frequency bands by micromachining. It is expected that our results will provide a platform for the study of low-dimensional topological phases, lossless photonic integrated circuits, and energy concentrators.

ACKNOWLEDGMENTS

Y.L. acknowledges support from National Natural Science Foundation of China (Grant No. 11874301). M.N.-C acknowledges support from the European Union's Horizon 2020 research and innovation program (Grant No. 777714).

[1] C. L. Kane and E. J. Mele, Quantum Spin Hall Effect in Graphene, Phys. Rev. Lett. **95**, 226801 (2005).

[2] B. A. Bernevig, T. L. Hughes, and S. C. Zhang, Quantum spin Hall effect and topological phase transition in HgTe quantum wells, Science **314**, 1757 (2006).

[3] M. Z. Hasan and C. L. Kane, Colloquium: Topological insulators, Rev. Mod. Phys. **82**, 3045 (2010).

[4] X. L. Qi and S. C. Zhang, Topological insulators and superconductors, Rev. Mod. Phys. **83**, 1057 (2011).

[5] L. H. Wu and X. Hu, Scheme for Achieving a Topological Photonic Crystal by Using Dielectric Material, Phys. Rev. Lett. **114**, 223901 (2015).

[6] L. Xu, H. X. Wang, Y. D. Xu, H. Y. Chen, and J. H. Jiang, Accidental degeneracy in photonic bands and topological phase transitions in two-dimensional core-shell dielectric photonic crystals, Opt. Express **24**, 18059 (2016).

[7] S. Mittal, V. Vikram Orre, G. Zhu, M. A. Gorlach, A. Poddubny, and M. Hafezi, Photonic quadrupole topological phases, Nat. Photonics **13**, 692 (2019).

[8] T. Ozawa, H. M. Price, A. Amo, N. Goldman, M. Hafezi, L. Lu, M. C. Rechtsman, D. Schuster, J. Simon, O. Zilberberg, and I. Carusotto, Topological photonics, Rev. Mod. Phys. **91**, 015006 (2019).

[9] C. W. Peterson, W. A. Benalcazar, T. L. Hughes, and G. Bahl, A quantized microwave quadrupole insulator with topologically protected corner states, Nature (London) **555**, 346 (2018).

[10] B. Y. Xie, G. X. Su, H. F. Wang, H. Su, X. P. Shen, P. Zhan, M. H. Lu, Z. L. Wang, and Y. F. Chen, Visualization of Higher-Order Topological Insulating Phases in Two-Dimensional Dielectric Photonic Crystals, Phys. Rev. Lett. **122**, 233903 (2019).

[11] Y. Liu, S. Leung, F. F. Li, Z. K. Lin, X. Tao, Y. Poo, and J. H. Jiang, Bulk-disclination correspondence in topological crystalline insulators, Nature (London) **589**, 381 (2021).

[12] S. Imhof, C. Berger, F. Bayer, J. Brehm, L. W. Molenkamp, T. Kiessling, F. Schindler, C. H. Lee, M. Greiter, T. Neupert, and R. Thomale, Topolectrical-circuit realization of topological corner modes, Nat. Phys. **14**, 925 (2018).

[13] S. M. Rafi-Ul-Islam, Z. B. Siu, and M. B. A. Jalil, Non-Hermitian topological phases and exceptional lines in topolectrical circuits, New J. Phys. **23**, 033014 (2021).
[14] M. Serra-Garcia, V. Peri, R. Süsstrunk, O. R. Bilal, T. Larsen, L. G. Villanueva, and S. D. Huber, Observation of a phononic quadrupole topological insulator, Nature (London) **555**, 342 (2018).
[15] Z. G. Chen, X. Ni, Y. Wu, C. He, X. C. Sun, L. Y. Zheng, M. H. Lu, and Y. F. Chen, Accidental degeneracy of double Dirac Cones in a phononic crystal, Sci. Rep. **4**, 4613 (2014).
[16] Z. J. Yang, F. Gao, X. H. Shi, X. Lin, Z. Gao, Y. D. Chong, and B. L. Zhang, Topological Acoustics, Phys. Rev. Lett. **114**, 114301 (2015).
[17] M. Xiao, G. Ma, Z. Yang, P. Sheng, Z. Q. Zhang, and C. T. Chan, Geometric phase and band inversion in periodic acoustic systems, Nat. Phys. **11**, 240 (2015).
[18] F. Sepehripour, P. Karimi, and A. Khavasi, Wideband and polarization-independent antireflection coating using metamaterials, IET. Optoelectron. **14**, 266 (2020).
[19] M. Ezawa, Higher-Order Topological Insulators and Semimetals on the Breathing Kagome and Pyrochlore Lattices, Phys. Rev. Lett. **120**, 026801 (2018).
[20] X. Zhang, H. X. Wang, Z. K. Lin, Y. Tian, B. Xie, M. H. Lu, Y. F. Chen, and J. H. Jiang, Second-order topology and multidimensional topological transitions in sonic crystals, Nat. Phys. **15**, 582 (2019).
[21] X. D. Chen, W. M. Deng, F. L. Shi, F. L. Zhao, M. Chen, and J. W. Dong, Direct Observation of Corner States in Second-Order Topological Photonic Crystal Slabs, Phys. Rev. Lett. **122**, 233902 (2019).
[22] H. Fan, B. Xia, L. Tong, S. Zheng, and D. Yu, Elastic Higher-Order Topological Insulator with Topologically Protected Corner States, Phys. Rev. Lett. **122**, 204301 (2019).
[23] M. Li, D. Zhirihin, M. Gorlach, X. Ni, D. Filonov, A. Slobozhanyuk, A. Alù, and A. B. Khanikaev, Higher-order topological states in photonic kagome crystals with long-range interactions, Nat. Photonics **14**, 89 (2020).
[24] W. Zhang, D. Zou, Q. Pei, W. He, J. Bao, H. Sun, and X. Zhang, Experimental Observation of Higher-Order Topological Anderson Insulators, Phys. Rev. Lett. **126**, 146802 (2021).
[25] A. Rycerz, J. Tworzydlo, and C. W. J. Beenakker, Valley filter and valley valve in graphene, Nat. Phys. **3**, 172 (2007).
[26] D. Xiao, W. Yao, and Q. Niu, Valley-Contrasting Physics in Graphene: Magnetic Moment and Topological Transport, Phys. Rev. Lett. **99**, 236809 (2007).
[27] Z. H. Qiao, W. K. Tse, H. Jiang, Y. G. Yao, and Q. Niu, Two-Dimensional Topological Insulator State and Topological Phase Transition in Bilayer Graphene, Phys. Rev. Lett. **107**, 256801 (2011).
[28] F. Zhang, A. H. MacDonald, and E. J. Mele, Valley Chern numbers and boundary modes in gapped bilayer graphene, Proc. Natl Acad. Sci. USA **110**, 10546 (2013).
[29] L. Ju, Z. W. Shi, T. Nair N, Y. C. Lv, C. H. Jin, J. Velasco, C. Ojeda-Aristizabal, H. A. Bechtel, M. C. Martin, A. Zettl, J. Analytis, and F. Wang, Topological valley transport at bilayer graphene domain walls, Nature (London) **520**, 650 (2015).
[30] J. Lu, C. Qiu, M. Ke, and Z. Liu, Valley Vortex States in Sonic Crystals, Phys. Rev. Lett. **116**, 093901 (2016).
[31] J. W. Dong, X. D. Chen, H. Zhu, Y. Wang, and X. Zhang, Valley photonic crystals for control of spin and topology, Nat. Mater. **16**, 298 (2017).
[32] J. Lu, C. Qiu, L. Ye, X. Fan, M. Ke, F. Zhang, and Z. Liu, Observation of topological valley transport of sound in sonic crystals, Nat. Phys. **13**, 369 (2017).
[33] X. T. He, E. T. Liang, J. J. Yuan, H. Y. Qiu, X. D. Chen, F. L. Zhao, and J. W. Dong, A silicon-on-insulator slab for topological valley transport, Nat. Commun. **10**, 872 (2019).
[34] S. Wong, M. Saba, O. Hess, and S. S. Oh, Gapless unidirectional photonic transport using all-dielectric kagome lattices, Phys. Rev. Res. **2**, 012011(R) (2020).
[35] J. K. Yang, Y. Hwang, and S. S. Oh, Evolution of topological edge modes from honeycomb photonic crystals to triangular-lattice photonic crystals, Phys. Rev. Res. **3**, L022025 (2021).
[36] J. Noh, S. Huang, K. P. Chen, and M. C. Rechtsman, Observation of Photonic Topological Valley Hall Edge States, Phys. Rev. Lett. **120**, 063902 (2018).
[37] X. Zhang, L. Liu, M. H. Lu, and Y. F. Chen, Valley-Selective Topological Corner States in Sonic Crystals, Phys. Rev. Lett. **126**, 156401 (2021).
[38] Y. H. Liu, H. L. Ren, L. Y. Tao, L. L. Du, X. Zhou, M. Z. Li, K. Song, R. N. Ji, X. P. Zhao, and M. Navarro-Cía, Mechanically-reconfigurable edge states in an ultrathin valley-hall topological metamaterial, Adv. Mater. Interfaces **9**, 2200998 (2022).
[39] D. Xiao, M. C. Chang, and Q. Niu, Berry phase effects on electronic properties, Rev. Mod. Phys. **82**, 1959 (2010).
[40] H. X. Wang, G. Y. Guo, and J. H. Jiang, Band topology in classical waves: Wilson-loop approach to topological numbers and fragile topology, New J. Phys. **21**, 093029 (2019).